Editors' Suggestion

Spin-wave reservoir chips with short-term memory for high-speed estimation of external magnetic fields

Sho Nagase,[1] Shoki Nezu,[1] and Koji Sekiguchi[2,3,4,*]

[1] *Graduate School of Engineering Science, Yokohama National University, Tokiwadai 79-5, Yokohama 240-8501, Japan*

[2] *Institute of Advanced Science, Yokohama National University, Tokiwadai 79-5, Yokohama 240-8501, Japan*

[3] *Institute of Multidisciplinary Sciences, Yokohama National University, Tokiwadai 79-5, Yokohama 240-8501, Japan*

[4] *Faculty of Engineering, Yokohama National University, Tokiwadai 79-5, Yokohama 240-8501, Japan*

(Received 23 March 2024; revised 17 June 2024; accepted 29 July 2024; published 29 August 2024)

The experimental realization of a spin-wave reservoir chip employing ferromagnetic permalloy thin films is presented. The novel device facilitates the interference of three spherical wave-excited surface mode spin waves within a rectangular waveguide via strategically positioned slits, enabling the detection of electrical signals from surface mode spin waves across all four observation antennas. Through the experiments conducted, it is confirmed that the device functions as a one-input, four-output reservoir capable of estimating external magnetic fields. Notably, the results demonstrate the device's capacity to retain memory up to one step prior in short-term memory tasks, while confirming the effectiveness of spin-wave interference induced by Huygens slits in enhancing nonlinearity, as observed in parity-check tasks. Furthermore, the inclusion of additional detection antennas contributes to improved learning accuracy, highlighting the significant progress achieved by the spin-wave reservoir chip. These findings underscore substantial progress toward practical implementation, with promising avenues for further development and refinement, showing its remarkable ability to process signals at high speeds, even with 0.8-ns pulse sequences.

DOI: 10.1103/PhysRevApplied.22.024072

I. INTRODUCTION

Physical reservoir computing is a novel information processing method [1,2]. Initially derived from recurrent neural networks, which typically comprise input, middle, and output layers, reservoir computing introduces a distinctive element known as the reservoir in its architecture [3–5]. Unlike traditional setups, the reservoir incurs no learning cost for establishing the weights of connections (synapses) among all neurons. The synapse weights are initially assigned arbitrary values, with only the output data from the reservoir undergoing training. The reservoir's primary function is to nonlinearly transform input data into higher dimensions, facilitating faster and energy-efficient information processing [5–9]. Nonlinear transformation can be achieved not only through computational processes using conventional electric circuits but also by leveraging certain physical phenomena. This is because specific physical phenomena inherently exhibit nonlinearity and short-term memory, both of which serve as alternatives to extensive learning computations. To date, physical reservoirs utilizing photonic microcavities, quantum bits, spin dynamics, and spin waves have been proposed as circuit-free and energy-efficient reservoirs [10–22].

Among these options, spin-wave physics offers a straightforward reservoir architecture since it operates in ambient air and at room temperature [23–27]. The groundbreaking spin-wave reservoir concept was introduced by Nakane [11], utilizing yttrium iron garnet (YIG) [28]. In this setup, nonlinear reservoir operations were executed through spin-wave interference. This research demonstrated that spin waves enable wire-free computation between input signals, and the voltage-controlled magnetic anisotropy (VCMA) effect of YIG played a crucial role as the source of spin-wave excitations [29–31]. It is noteworthy, however, that achieving VCMA in ferrimagnetic insulator YIG remained elusive. Recently, an alternative spin-wave reservoir concept has been put forward, which proposes the utilization of standing spin waves in a magnetic disk to create a reciprocal space reservoir [32]. In this arrangement, Brillouin light scattering spectroscopy, a large optical system, plays a crucial role in configuring the reservoir system. Nevertheless, it is

*Contact author: sekiguchi-koji-gb@ynu.ac.jp

important to note that, even within this system, the concrete realization of a spin-wave reservoir as a chip device has not yet been accomplished.

In this study, we investigated the fundamental behaviors of a spin-wave reservoir chip electrically. Nonlinear spin waves were generated using an electric antenna in conjunction with the Huygens principle. Independent detection antennas captured the signals of complexly interfered spin waves in the time domain. Through the analysis of spin-wave signals, we examined basic computational tasks to validate reservoir performance, namely, short-term memory (STM) and parity-check (PC) tasks. Our demonstrated prototypes significantly improved the capability of reservoir computation, enabling a more expanded architecture such as multiple inputs and multiple outputs devices. In addition, an all-electric detection chip device shows potential as an edge computing reservoir chip, as it eliminates the need for unrealized VCMA of YIG and avoids large optical systems.

II. RESULTS AND DISCUSSION

Figure 1 depicts a schematic of the experimental setup. The spin-wave reservoir consisted of permalloy (Py) sputtered 300 nm onto a Si substrate with a 100-nm-insulating SiO_2 layer. The reservoir was fabricated using the Ar ion milling method into a rectangular shape with a width (w) of 40 μm and a length (l) of 80 μm. To maintain the sample's flatness, an insulating SiO_2 layer was used for backfilling. The spin-wave excitation antenna and detection antennas were sputtered with Ti (5 nm)/Au (200 nm), as depicted in Fig. 1(a). The excitation antenna was a coplanar waveguide (CPW) in a ground-signal-ground through configuration, while the detection antennas were asymmetric CPWs. The CPWs were designed to have a characteristic impedance of 50 Ω, and the separation distance between the signal-ground line was designed to be 2.15 μm. All antennas were made with 3-μm-wide wires. Figure 1(b) illustrates the detailed structure of the spin-wave reservoir, featuring two independent slits positioned beneath the excitation antenna to induce complex spin-wave interference according to the Huygens principle. Each slit measured 2 μm in width and 3 μm in length. Additionally, four independent antennas surround the slits (four-port spin-wave reservoir). Figures 1(c) and 1(d) represent the reference reservoir without slits, which was utilized to demonstrate the heightened nonlinearity observed in the sample depicted in Fig. 1(b).

As shown in Fig. 1(e), spin waves were excited by an excitation antenna launching a fast pulse using a pulse generator (Picosecond Pulse Labs 10070A). The excitation pulse had a duration of 10 nm and an amplitude of 7 V; the repetition frequency was 100 kHz. An external magnetic field H_y was applied parallel to the y-axis, and the signals of the spin waves were detected by detection antennas connected to a sampling oscilloscope (Agilent Technologies DCA-J 86100C). The opposite ends of both the excitation and detection transmission lines were connected to a low-noise ground. The measured signal $V(H_y)$ was composed of the spin-wave amplitude V_{sw} and background noise V_n and can be represented as $V(H_y) = V_{sw} + V_n$. To eliminate the field-independent background noise V_n, the zero-field data $V(0) = V_n$ was subtracted [33–35].

TABLE I. Hyperparameters and a function for machine learning.

Learning rate η	Epochs	Threshold θ	Activation function
0.7	4000	0	$f(x) = 1/[1 + \exp(-x)]$

To explore the fundamental potential of the physical reservoir, the spin-wave reservoir was utilized to estimate the applied external magnetic field. The bias magnetic field was set at $H_y = 600$ Oe, while an additional magnetic field was applied parallel to the x-axis. Consequently, the external field became the vector sum of $\boldsymbol{H}_{ext} = \boldsymbol{H}_y + \boldsymbol{H}_x$. The spin-wave primarily propagates as a magnetostatic surface spin-wave (MSSW) but undergoes modulation by H_x, exhibiting a mixed character with a backward volume magnetostatic spin-wave. Figures 1(f)–1(i) illustrate the spin-wave waveforms (reservoir output) detected by four independent antennas labeled 1 to 4 when $H_x = 10$ Oe, which contain peculiar features. Note that the spin-wave reservoir does not require a circuit to generate nonlinear transformations. To extract the features, we have adopted four steps of signal processing: (1) digital Fourier filtering (bandpass $7 < f < 11.5$ GHz) to reduce noise, (2) Hilbert transformation to extract characteristic envelopes, (3) up-sampling of discrete data with a 0.01-ns resolution to be set at 500 points, and (4) machine (supervised) learning by the gradient descent method choosing certain successive 20 points [Appendix A]. The hyperparameters and an activation function for machine learning are summarized in Table I. The envelopes at $H_x = 30$, 50, 70, and 90 Oe were used as the training dataset, while the envelopes at $H_x = 20$, 40, 60, and 80 Oe were used as the test dataset.

Figure 1(j) represents the learning accuracy of H_x using the spin-wave reservoir. In an ideal scenario where the spin-wave reservoir achieves perfect learning accuracy, the estimated magnetic field values should align with the black solid line labeled "Answer." Given that H_x was experimentally varied at intervals of 10 Oe, machine learning was considered successful when the root mean square error (RMSE) remained within ±5 Oe [11,13,36]. As depicted by the blue and red solid circles, the trained and learned data points are closely distributed around the "Answer" line. The RMSE of the learning dataset was

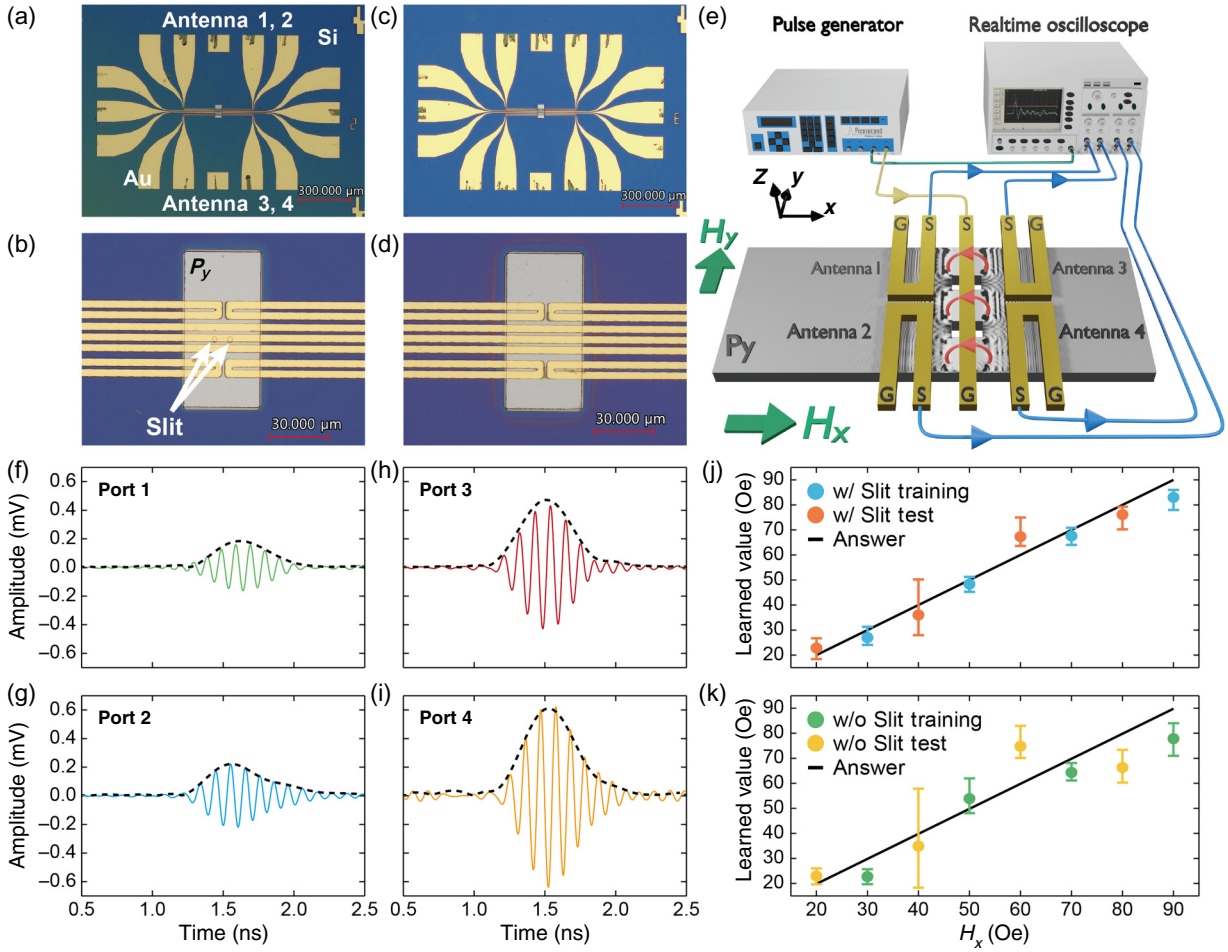

FIG. 1. Schematic illustration of the spin-wave reservoir chip and the experimental setup. (a) A spin-wave reservoir fabricated using permalloy thin films. (b) Two independent slits fabricated beneath the CPW excitation antenna, which connects to the pulse generator. Four independent antennas surround the two slits and are numbered from 1 to 4. (c) Reference sample. (d) Spin-wave reservoir without any slits. (e) Spin-wave signals detected using a sampling oscilloscope. Here, to excite the surface-spin wave mode, bias magnetic fields are applied along the y-axis, while small modulation fields are applied parallel to the x-axis. A simulated wave front is inserted at the surface of the Py thin film. (f)–(i) Spin-wave waveforms detected in the time domain using antennas 1 through 4. Each packet forms a characteristic envelope indicated by dashed lines. (j) External field estimation using a spin-wave reservoir with slits. (k) External field estimation using the reference reservoir without slits.

2.953, whereas that of the test dataset was 4.670. Consequently, the estimation of H_x was successfully accomplished. To understand the effect of nonlinear interference on learning accuracy, the magnetic field estimation was also performed using the reference reservoir sample shown in Fig. 1(d), which contains no slits. Figure 1(k) illustrates the result of the same task of estimating the magnetic field H_x and displays an RMSE value of 9.110 for the test dataset, indicating significantly poorer accuracy. The slits contribute to the increase of features, resulting in more accurate machine learning.

The magnetic field estimation presented above was not sufficient to demonstrate that the spin-wave reservoir was a powerful physical reservoir. To validate this claim, we conducted tests on the well-known benchmark tasks known as short-term memory (STM) and parity-check (PC) tasks [13,16,30,37] using high-speed pulse sequences. As explained in a major textbook on machine learning, the important metrics of STM for certain time-series data $x(n)$ ($n = 1, 2, 3, \ldots$) are the square of the correlation coefficient r and learning capacity C_{STM} [36], so that

$$r^2(\tau) = \frac{C_{\mathrm{ov}}^2(y(n), y_{\mathrm{STM}}(n,\tau))}{C_{\mathrm{ov}}(y(n))C_{\mathrm{ov}}(y_{\mathrm{STM}}(n,\tau))}, \tag{1}$$

$$C_{\mathrm{STM}} = \sum_{\tau=0} r^2(\tau). \tag{2}$$

The output y_{STM} to be predicted is given by the equation $y_{\mathrm{STM}}(n,\tau) = x(n-\tau)$, where n represents the current time

step and τ denotes the number of time steps to look back. The $C_{\mathrm{ov}}(x,\ y)$ is the covariance. If the $r^2(\tau)$ is close to 1, it indicates a strong correlation with the ideal output, thus indicating high learning accuracy. The larger value of C_{STM} indicates a better reservoir. The STM task is a good indicator of capability for tracking history [36]. Similarly, the critical metrics for the parity-check task are given as follows:

$$r^2(\tau) = \frac{C_{\mathrm{ov}}^2(y(n), y_{\mathrm{PC}}(n,\tau))}{C_{\mathrm{ov}}(y(n))C_{\mathrm{ov}}(y_{\mathrm{PC}}(n,\tau))}, \tag{3}$$

$$C_{\mathrm{PC}} = \sum_{\tau=0} r^2(\tau). \tag{4}$$

The output y_{PC} (to be predicted) is given by the equation $y_{\mathrm{PC}}(n,\tau) = x(n) \oplus x(n-1) \oplus \ldots \oplus x(n-\tau)$ where n represents the current time step and τ denotes the number of time steps to look back. The operator $\oplus$ represents the exclusive or (XOR) operator. Note that the PC task serves as an indicator that captures both the ability to track history and nonlinearity simultaneously since the calculation of XOR is not linearly separable; thus, it requires the ability to perform nonlinear computational processing.

Figure 2 shows an experimental setup for the STM and PC tasks of the spin-wave reservoir. As shown in Fig. 2(a), the excitation antenna was connected to an arbitrary wave generator (Tektronix AWG70002A), and the detection antennas were connected to a real-time oscilloscope (Agilent DSO80604B) to deal with a long data length. The spin-wave signal was averaged over 65534 waveforms. As depicted in Fig. 2(b), the random 500-bit pattern, e.g., 101000110110…, was converted into an electric pulse train at the input layer. Each pulse has a duration of 0.8 ns, and the train comprises a total of 500 pulses. The offset voltage was set at −250 mV. A signal of "1" was designated as +250 mV, and a signal of "0" was set to approximately one-third of the signal "1," which was about 83 mV. Subsequently, the electric pulse train generates spin waves and induces nonlinear interference via the slits, ultimately mapping to higher dimensions. The physical reservoir layer generates intricate spin-wave patterns. The spin-wave waveforms from the 101st to the 300th pattern (step) were used for the training dataset, while patterns 301 to 500 were used for the test dataset. We have adopted four steps of signal processing in the read-out layer shown in Fig. 2(b): (1) digital Fourier filtering (bandpass $4 < f < 8$ GHz) to reduce noise, (2) Hilbert transformation to extract characteristic envelopes, (3) upsampling of discrete data with a 0.01-ns resolution to create 80 points for each spin-wave envelope (0.8 ns/0.01 ns), and (4) machine learning was conducted to estimate initial

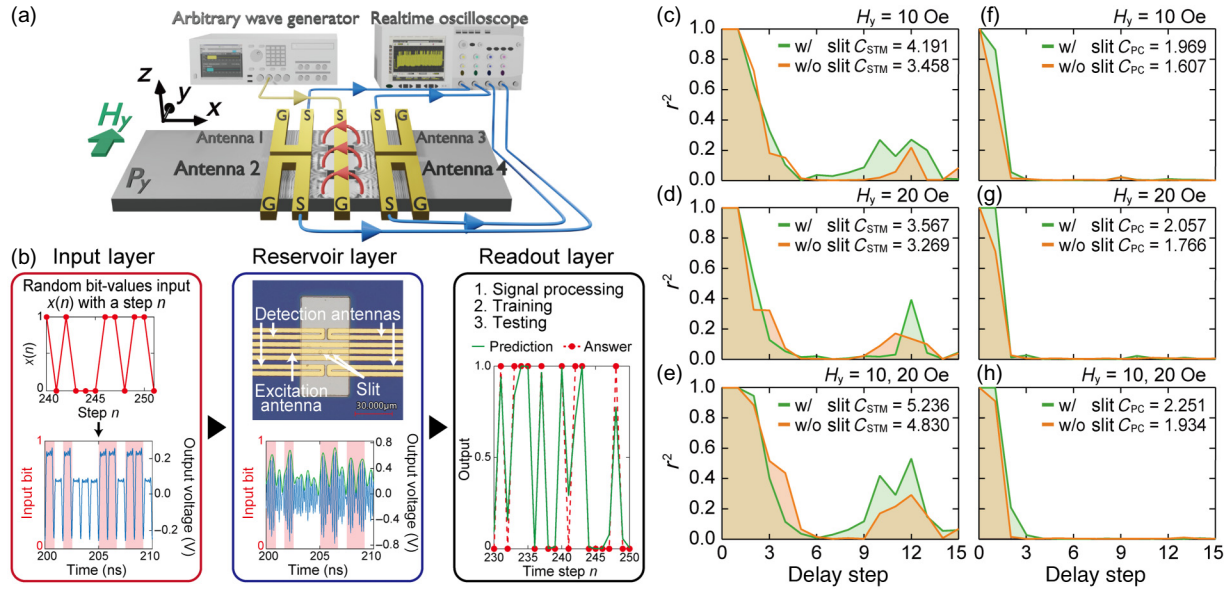

FIG. 2. Experimental setup for the short-term memory and parity-check tasks of the four-port spin-wave reservoir. (a) Excitation antenna connected to the arbitrary wave generator. Here, detection antennas connect to a real-time oscilloscope. (b) Layout of the spin-wave reservoir. Time-series data involves 500 random bits that convert into a continuous-electric 500-pulse train at the input layer. These pulse trains generate nonlinearly interfered spin waves in the permalloy thin film at the reservoir layer. The read-out layer creates the training dataset and performs machine learning. The evaluated C_{STM} for three different datasets: (c) $\{\boldsymbol{v}_{\mathrm{port1}}$ ($H_y = 10$ Oe), …, $\boldsymbol{v}_{\mathrm{port4}}$ ($H_y = 10$ Oe)$\}$, (d) $\{\boldsymbol{v}_{\mathrm{port1}}$ ($H_y = 20$ Oe), …, $\boldsymbol{v}_{\mathrm{port4}}$ ($H_y = 20$ Oe)$\}$, and (e) $V\{\boldsymbol{v}_{\mathrm{port1}}$ ($H_y = 10$ Oe), …, $\boldsymbol{v}_{\mathrm{port4}}$ ($H_y = 10$ Oe), $\boldsymbol{v}_{\mathrm{port1}}$ ($H_y = 20$ Oe), …, $\boldsymbol{v}_{\mathrm{port4}}$ ($H_y = 20$ Oe)$\}$. The evaluated C_{PC} for three different datasets: (f) $\{\boldsymbol{v}_{\mathrm{port1}}$ ($H_y = 10$ Oe), …, $\boldsymbol{v}_{\mathrm{port4}}$ ($H_y = 10$ Oe)$\}$, (g) $\{\boldsymbol{v}_{\mathrm{port1}}$ ($H_y = 20$ Oe), …, $\boldsymbol{v}_{\mathrm{port4}}$ ($H_y = 20$ Oe)$\}$, and (h) $\{\boldsymbol{v}_{\mathrm{port1}}$ ($H_y = 10$ Oe), …, $\boldsymbol{v}_{\mathrm{port4}}$ ($H_y = 10$ Oe), $\boldsymbol{v}_{\mathrm{port1}}$ ($H_y = 20$ Oe), …, $\boldsymbol{v}_{\mathrm{port4}}$ ($H_y = 20$ Oe)$\}$.

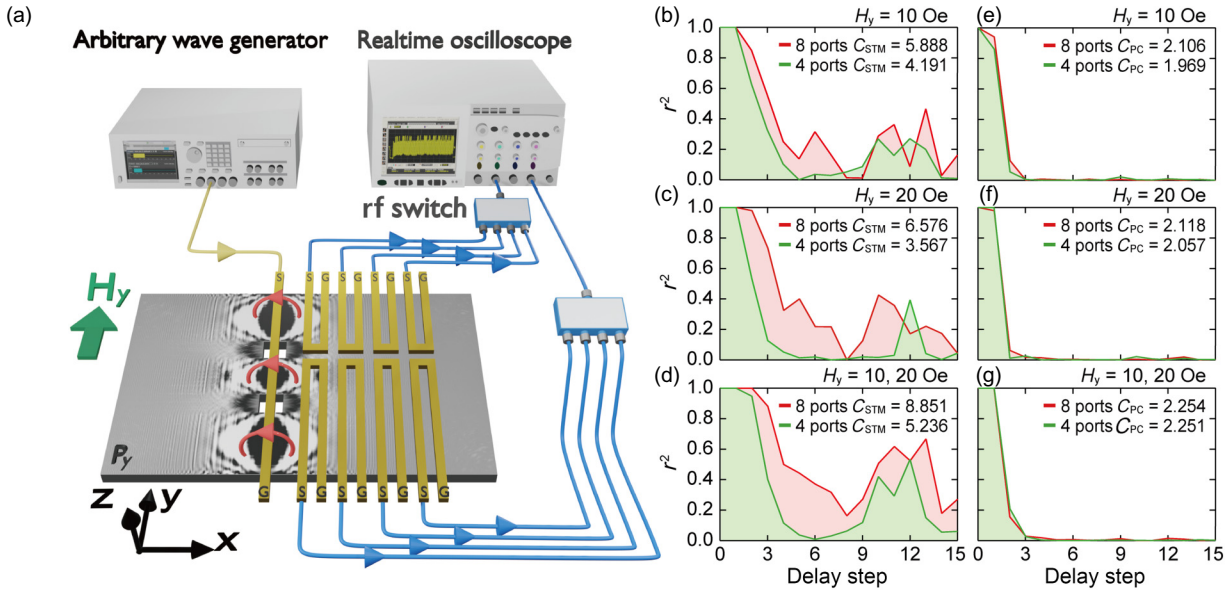

FIG. 3. Experimental setup for the short-term memory and parity-check tasks of the eight-port spin-wave reservoir. (a) Spin-wave excited by an arbitrary wave generator. A simulated wave front is inserted at the surface of the Py thin film. Here, spin-wave signals are detected by eight antennas placed at different positions using real-time oscilloscope via rf switches at the maximum 40 GS/s sampling. The evaluated C_{STM} for three different datasets: (b) $\{\boldsymbol{v}_{\mathrm{port1}}\ (H_y = 10\ \mathrm{Oe}), \ldots, \boldsymbol{v}_{\mathrm{port8}}\ (H_y = 10\ \mathrm{Oe})\}$, (c) $\{\boldsymbol{v}_{\mathrm{port1}}\ (H_y = 20\ \mathrm{Oe}), \ldots, \boldsymbol{v}_{\mathrm{port8}}\ (H_y = 20\ \mathrm{Oe})\}$, and (d) $V\{\boldsymbol{v}_{\mathrm{port1}}\ (H_y = 10\ \mathrm{Oe}), \ldots, \boldsymbol{v}_{\mathrm{port8}}\ (H_y = 10\ \mathrm{Oe}), \boldsymbol{v}_{\mathrm{port1}}\ (H_y = 20\ \mathrm{Oe}), \ldots, \boldsymbol{v}_{\mathrm{port8}}\ (H_y = 20\ \mathrm{Oe})\}$. The evaluated C_{PC} for three different datasets: (e) $\{\boldsymbol{v}_{\mathrm{port1}}\ (H_y = 10\ \mathrm{Oe}), \ldots, \boldsymbol{v}_{\mathrm{port8}}\ (H_y = 10\ \mathrm{Oe})\}$, (f) $\{\boldsymbol{v}_{\mathrm{port1}}\ (H_y = 20\ \mathrm{Oe}), \ldots, \boldsymbol{v}_{\mathrm{port8}}\ (H_y = 20\ \mathrm{Oe})\}$, and (g) $\{\boldsymbol{v}_{\mathrm{port1}}\ (H_y = 10\ \mathrm{Oe}), \ldots, \boldsymbol{v}_{\mathrm{port8}}\ (H_y = 10\ \mathrm{Oe}), \boldsymbol{v}_{\mathrm{port1}}\ (H_y = 20\ \mathrm{Oe}), \ldots, \boldsymbol{v}_{\mathrm{port8}}\ (H_y = 20\ \mathrm{Oe})\}$.

bit patterns using the middle 16 points of each spin-wave envelope. The Ridge regression method was used to mitigate overfitting, with a regularization parameter (λ) set to 0.1 [Appendix B]. Hereafter, we use the terminology "port" to distinguish the function of the read-out layer from the "antenna," which refers to the physical reservoir layer.

The STM and PC tasks were demonstrated using three datasets: $\{\boldsymbol{v}_{\mathrm{port1}}\ (H_y = 10\ \mathrm{Oe}), \ldots, \boldsymbol{v}_{\mathrm{port4}}\ (H_y = 10\ \mathrm{Oe})\}$, $\{\boldsymbol{v}_{\mathrm{port1}}\ (H_y = 20\ \mathrm{Oe}), \ldots, \boldsymbol{v}_{\mathrm{port4}}\ (H_y = 20\ \mathrm{Oe})\}$, and the virtual node dataset $\{\boldsymbol{v}_{\mathrm{port1}}\ (H_y = 10\ \mathrm{Oe}), \ldots, \boldsymbol{v}_{\mathrm{port4}}\ (H_y = 10\ \mathrm{Oe}), \boldsymbol{v}_{\mathrm{port1}}\ (H_y = 20\ \mathrm{Oe}), \ldots, \boldsymbol{v}_{\mathrm{port4}}\ (H_y = 20\ \mathrm{Oe})\}$ where the data for 20 Oe are treated as virtual additional ports. Figures 2(c)–2(e) show the learning capacities of C_{STM} and Figs. 2(f)–2(h) display C_{PC} for these datasets. An ideal superior reservoir should exhibit a robust correlation ($r^2(\tau) = 1$) and maintain it over extended delay steps (from 0 to 15). In the case of dataset $\{\boldsymbol{v}_{\mathrm{port1}}\ (H_y = 10\ \mathrm{Oe}), \ldots, \boldsymbol{v}_{\mathrm{port4}}\ (H_y = 10\ \mathrm{Oe})\}$, which is shown by the green color in Fig. 2(c), the four-port spin-wave reservoir with slits exhibits a finite correlation $r^2(\tau)$ up to the 4th step and loses correlation at the 5th step. Interestingly, the spin-wave reservoir regains correlation at the 9th to 13th steps. The C_{STM} was evaluated as 4.191. This pattern is consistent with dataset $\{\boldsymbol{v}_{\mathrm{port1}}\ (H_y = 20\ \mathrm{Oe}), \ldots, \boldsymbol{v}_{\mathrm{port4}}\ (H_y = 20\ \mathrm{Oe})\}$ shown in Fig. 2(d), where the C_{STM} was evaluated as 3.567. The virtual node dataset $\{\boldsymbol{v}_{\mathrm{port1}}\ (H_y = 10\ \mathrm{Oe}), \ldots, \boldsymbol{v}_{\mathrm{port4}}\ (H_y = 10\ \mathrm{Oe}), \boldsymbol{v}_{\mathrm{port1}}\ (H_y = 20\ \mathrm{Oe}), \ldots, \boldsymbol{v}_{\mathrm{port4}}\ (H_y = 20\ \mathrm{Oe})\}$ depicted in Fig. 2(e) exhibits an improved learning capacity, with $C_{\mathrm{STM}} = 5.236$. Compared with the result of the reference reservoir (without slits) shown in red ($C_{\mathrm{STM}} = 3.458$, 3.269, and 4.830), the reservoir consistently maintains stronger correlations.

The STM task's physical interpretation suggests that the correlation from the 1st to 4th step originates from initial interfered spin waves, while the correlation from the 9th to 13th step is induced by the interference of spin waves reflected at the edges of the rectangular waveguide. The delay step corresponds to the propagation delay of spin waves. Fortunately, the finite scale of the permalloy rectangle increases the complicated spin-wave dynamics. The slits in permalloy film increase nonlinearity compared with the C_{STM} of the reference reservoir for each dataset [the effect of slits is described in Appendix C]. Regarding the evaluated C_{PC} depicted in Figs. 2(f)–2(h), the correlation extends up to the 2nd step, and C_{PC} remains consistently small across all datasets. The physical interpretation of the PC task suggests that the nonlinearity is not sufficiently strong under the current experimental conditions. As explained earlier, C_{PC} is more strongly influenced by the nonlinear computation of the XOR operation than by history tracking. Therefore, the C_{PC} of the four-port reservoir with slits consistently exceeds that of the reference reservoir without slits, with the minor difference indicating only a slight increase in nonlinearity in the presence

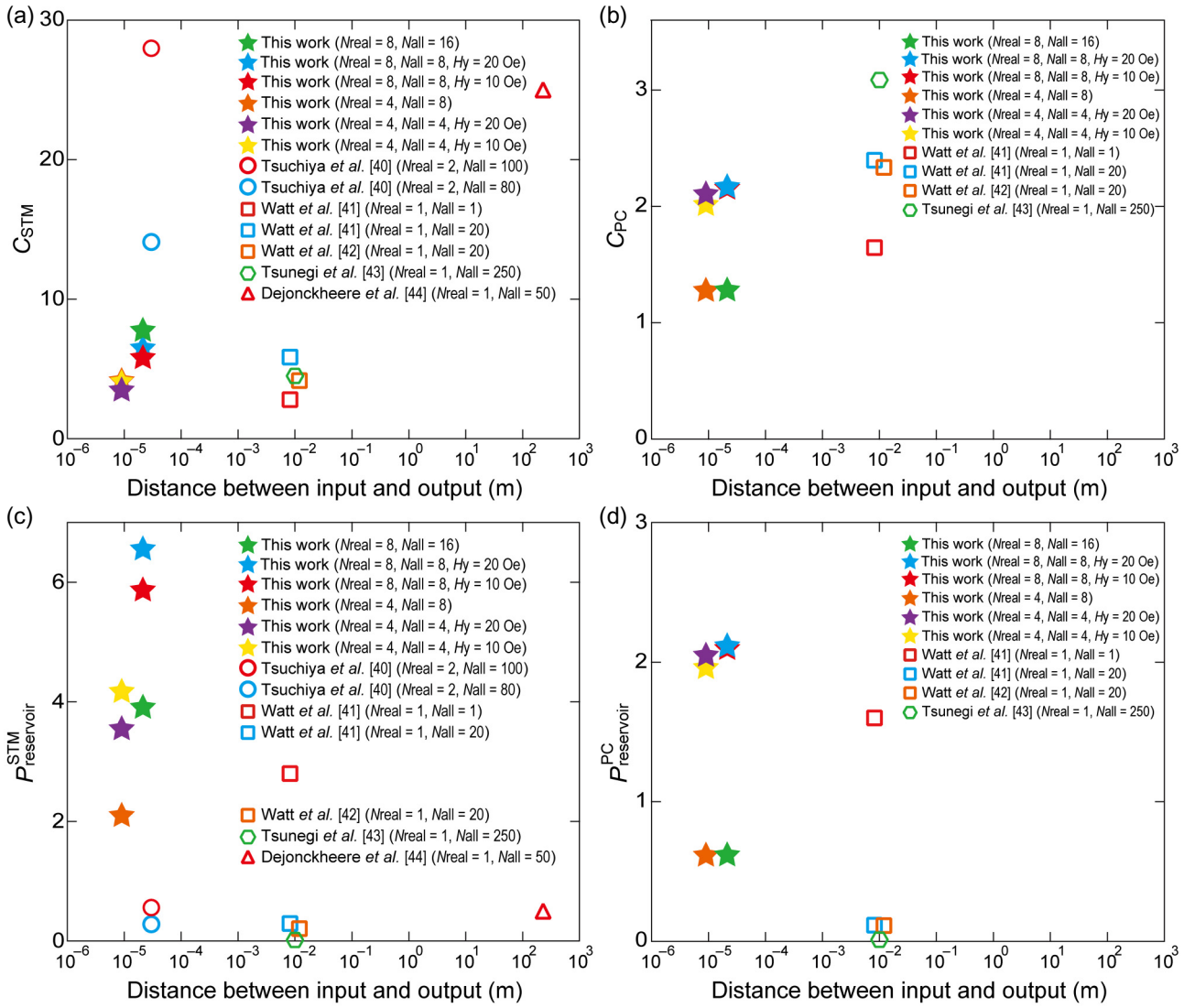

FIG. 4. Experimentally reported capabilities and performance indexes of the physical reservoirs. The experimentally reported values of (a) C_{STM} and (b) C_{PC}. The performance index of the (c) short-term memory $P^{STM}_{reservoir}$ and (d) parity-check $P^{PC}_{reservoir}$ tasks, as experimentally reported.

of the slits. Nonetheless, the magnitudes of C_{PC} exceed those of other physical reservoir systems. This point will be discussed later.

Eight-port spin-wave reservoir chips were fabricated to enhance the performance of the four-port reservoir, as depicted in Fig. 3(a). The reservoir was fabricated using the Ar ion milling method into a rectangular shape with a width (w) of 90 μm and a length (l) of 120 μm. Each slit measures 5 μm in width and 5 μm in length. The eight antennas were positioned off-center to amplify the nonlinearity caused by interference slits, while varying the distances between the eight antennas aimed to increase the features of the measured spin-wave envelope. The eight antennas were connected to a real-time oscilloscope via rf switches to maintain a maximum 40 GS/s sampling rate. The group velocity v_g of the MSSW in this device can be derived by differentiating the MSSW dispersion with respect to wavenumber k. Using the film thickness $d = 300$ nm and wavenumber $k = 0.37$ μm^{-1}, we obtain $v_g = 47.3$ km/s at an external magnetic field of 10 Oe and $v_g = 46.8$ km/s at 20 Oe. The propagation distances for each antenna are 10 μm, 17 μm, 25 μm, and 33 μm, starting from the input antenna. Consequently, it is observed that the spin waves detected by the closest and farthest antennas exhibit a time difference of approximately 0.65 ns. This corresponds to about 0.8 steps of the input signal from the random bit sequence. The STM and PC tasks followed the same scheme as the four-port spin-wave reservoir. Figure 3 shows the evaluations of the STM and PC tasks for the eight-port spin-wave reservoir chip. As shown in Figs.

3(b)–3(d), the correlation $r^2(\tau)$ shown in red was greatly improved for all the datasets and remained strong throughout all of the 15 steps; especially, at $C_{\mathrm{STM}} = 8.851$ for the virtual node dataset. As shown in Figs. 3(e)–3(g), the C_{PC} of the eight-port reservoir shown in red exceeds that of the four-port reservoir displayed in green, with a minor difference of less than 0.1 that indicates that the fundamental nonlinearity remains unchanged. However, the extracted features of the envelope were enhanced by positioning the eight antennas off-center.

Finally, it is important to discuss the performance of C_{STM} and C_{PC}. In Figs. 4(a) and 4(b), the reported values of C_{STM} and C_{PC} were summarized [38–42]. However, it is crucial to note that the reported values of C_{STM} and C_{PC} in the reference papers are calculated by summing from delay step $\tau = 1$, whereas we sum from delay step $\tau = 0$. When comparing, it is necessary to adjust the method of summation to account for taking the sum from delay step $\tau = 0$ instead of delay step $\tau = 1$, which provides the appropriate values for comparison. For C_{STM} at delay step $\tau = 0$, which is 1, it corresponds to the operation of subtracting or adding 1. In the evaluation of the physical reservoir, two independent performances, namely, hardware and software (computation) performance, are important. Previous reports used the sophisticated computational technique of the virtual node method, which effectively increased the performance of C_{STM} and C_{PC}, as shown in Figs. 4(a) and 4(b). Within the scope of this study, we have concentrated solely on evaluating the performance of the physical hardware (device) itself. While increasing the number of virtual nodes (n_{virtual}) is theoretically possible by dedicating more time to experiments, this approach comes at the expense of increased computational costs and a subsequent decline in the performance of high-speed processing for real-time series signals. The usage of v_{irtual} obscures the evaluation of the true performance of the physical reservoir layer. As evident from our experiments, increasing the number of real nodes n_{real} improves the accuracy of feature acquisition without causing a rise in computational costs. Moreover, from the perspective of constructing a multi-input, multi-output physical reservoir, the value of n_{real} is crucial. It is then scientifically appropriate to define the performance indexes $P^{\mathrm{STM}}_{\mathrm{reservoir}}$ and $P^{\mathrm{PC}}_{\mathrm{reservoir}}$ for a comparison, which are given by

$$P^{\mathrm{STM}}_{\mathrm{reservoir}} = C_{\mathrm{STM}} \frac{n_{\mathrm{real}}}{n_{\mathrm{all}}}, \tag{5}$$

$$P^{\mathrm{PC}}_{\mathrm{reservoir}} = C_{\mathrm{PC}} \frac{n_{\mathrm{real}}}{n_{\mathrm{all}}}, \tag{6}$$

where $n_{\mathrm{all}} = n_{\mathrm{real}} + n_{\mathrm{virtual}}$. When $n_{\mathrm{virtual}} = 0$, Eqs. (5) and (6) simply indicate $P^{\mathrm{STM}}_{\mathrm{reservoir}} = C_{\mathrm{STM}}$ and $P^{\mathrm{PC}}_{\mathrm{reservoir}} = C_{\mathrm{PC}}$, since $n_{\mathrm{all}} = n_{\mathrm{real}}$, making them quite fair indexes. Figure 4 shows the experimentally reported $P^{\mathrm{STM}}_{\mathrm{reservoir}}$ and $P^{\mathrm{PC}}_{\mathrm{reservoir}}$ in relation to the scale of physical reservoir device. As clearly depicted in Fig. 4(c), the case of the highest performance of C_{STM} ($n_{\mathrm{real}} = 8$, $n_{\mathrm{all}} = 16$) with a value of 8.851 in this study exhibits a degradation in $P^{\mathrm{STM}}_{\mathrm{reservoir}}$ compared with the cases of C_{STM} ($n_{\mathrm{real}} = 4$, $n_{\mathrm{all}} = 4$) and C_{STM} ($n_{\mathrm{real}} = 8$, $n_{\mathrm{all}} = 8$). As shown in Figs. 4(c) and 4(d), the performance of both $P^{\mathrm{STM}}_{\mathrm{reservoir}}$ and $P^{\mathrm{PC}}_{\mathrm{reservoir}}$ in all cases studied here exceeds that of previous physical reservoirs. This indicates that the spin-wave reservoir offers advantages, such as the absence of wiring in the reservoir layer and scalability.

III. CONCLUSION

The experimental demonstration of the spin-wave reservoir chip utilized ferromagnetic permalloy thin films. We designed a spin-wave reservoir device capable of interfering with three spherical wave-excited surface mode spin waves in a rectangular waveguide via slits. Results from the spin-wave propagation experiment showed that electrical signals of surface mode spin waves were detectable at all four observation antennas. It was confirmed that the device functions as a one-input, four-output reservoir device capable of performing external magnetic field estimation tasks without using the virtual node method. Findings from the short-term memory task indicated that the device retains sufficient memory up to one step prior. Moreover, results from the parity-check task validated that spin-wave interference caused by slits effectively increases nonlinearity. The addition of detection antennas confirmed an improvement in learning accuracy resulting from higher dimensionality and increased short-term memory due to time differences in the signals detected from each antenna, which led to a significant enhancement in learning accuracy in the short-term memory task. Despite the anticipated improvement in learning accuracy through enhanced feature extraction due to antenna asymmetry, only marginal gains were observed in the parity-check task. This limited performance can be attributed to the inherent linearity of the system under low driving (excitation) energy, which is insufficient for the highly nonlinear transformation required by a parity check. The results of both the parity-check and short-term memory tasks obtained in this study outperform the performance of the other physical reservoirs reported to date. This indicates a step closer to practical implementation, with the potential for further extension.

The data supporting the findings of this study are available from the corresponding author upon reasonable request.

ACKNOWLEDGMENTS

This work 10.13039/100011440 was supported by Grants-in-Aid for Scientific Research (Grants No. 19H00861, No. 18H05346, and No. 22K18321) from the 10.13039/501100001691 Japan Society for the

Promotion of Science (10.13039/501100001691 JSPS). K. S. acknowledges the support of Grants-in-Aid for Scientific Research (Grant No. 20H05652).

S. N. and K. S. planned the experiments. S. N. and K. S. designed and prepared the samples and performed spin-wave reservoir measurements. S. N. performed the analysis of machine learning. S. N. and K. S. wrote the manuscript. All authors discussed the results.

The authors declare no competing financial interests.

APPENDIX A

Gradient descent method for field estimation

From the time-series data, we extracted 20 data points from the experimental data and stored the data in array $\boldsymbol{y}$. Here, $\boldsymbol{y} = (y_{\mathrm{port1}}, y_{\mathrm{port2}} \ldots, y_{\mathrm{port4}})^{\mathrm{T}}$ and its dimensions are 4×20. To estimate a hidden variable of $\boldsymbol{y}$, such as the external magnetic field H_{ext}, we associate the scalar $\bar{d} = (1/20)\sum f(\boldsymbol{W}^{\mathrm{out}}\boldsymbol{y} - \theta)$ with H_{ext} in the training process and determine the weight matrix $\boldsymbol{W}^{\mathrm{out}}$ until it minimizes the difference between targeted z and trained values $\bar{d}$. Using the error function $E = 1/2||(z - \bar{d})||^2$, the weight matrix is updated according to $\hat{\boldsymbol{W}}^{\mathrm{out}} = \boldsymbol{W}^{\mathrm{out}} - \eta\partial E/\partial \boldsymbol{W}^{\mathrm{out}}$. In the final testing procedure, using the prefixed weight matrix $\hat{\boldsymbol{W}}^{\mathrm{out}}$, the input values were predicted [11].

APPENDIX B

Ridge regression method

For the time-series data, we extracted the n-step data from the experimental data and stored the data in the array $\boldsymbol{y}(n)$. Here, $\boldsymbol{y}(n) = (y_{\mathrm{port1}}(n), y_{\mathrm{port2}}(n) \ldots y_{\mathrm{port8}}(n))^{\mathrm{T}}$. During the training process, we defined the answer array as $\boldsymbol{d}(n) = (d_1(n), d_2(n) \ldots d_8(n))^{\mathrm{T}}$. During the training process, we determined the weight matrix $\hat{\boldsymbol{W}}^{\mathrm{out}}$ that connects $\boldsymbol{y}(n)$ and $\boldsymbol{d}(n)$ as $\hat{\boldsymbol{W}}^{\mathrm{out}} = \boldsymbol{d}\boldsymbol{y}^{\mathrm{T}}(\boldsymbol{y}\boldsymbol{y}^{\mathrm{T}} + \lambda \boldsymbol{I})^{-1}$. In the final testing procedure, using the prefixed weight matrix $\hat{\boldsymbol{W}}^{\mathrm{out}}$, the input values were predicted as $\boldsymbol{z} = \hat{\boldsymbol{W}}^{\mathrm{out}}\boldsymbol{y}$ [36,43]. The dimensions of $\boldsymbol{z}$, $\hat{\boldsymbol{W}}^{\mathrm{out}}$, and $\boldsymbol{y}$ are $1 \times n$, 1×8, and $8 \times n$, respectively.

APPENDIX C

Effect of Huygens slits

Figure 5(a) shows the MUMAX3 simulation results for the magnetization of a four-port spin-wave reservoir [simulation method was described in Appendix D] [44]. The external magnetic field 10 Oe was applied parallel to the y-axis. Before launching the microwave current, magnetic domain walls are observed near the Huygens slits. On input of a 0.8-ns pulse current I_{in}, we obtained the time

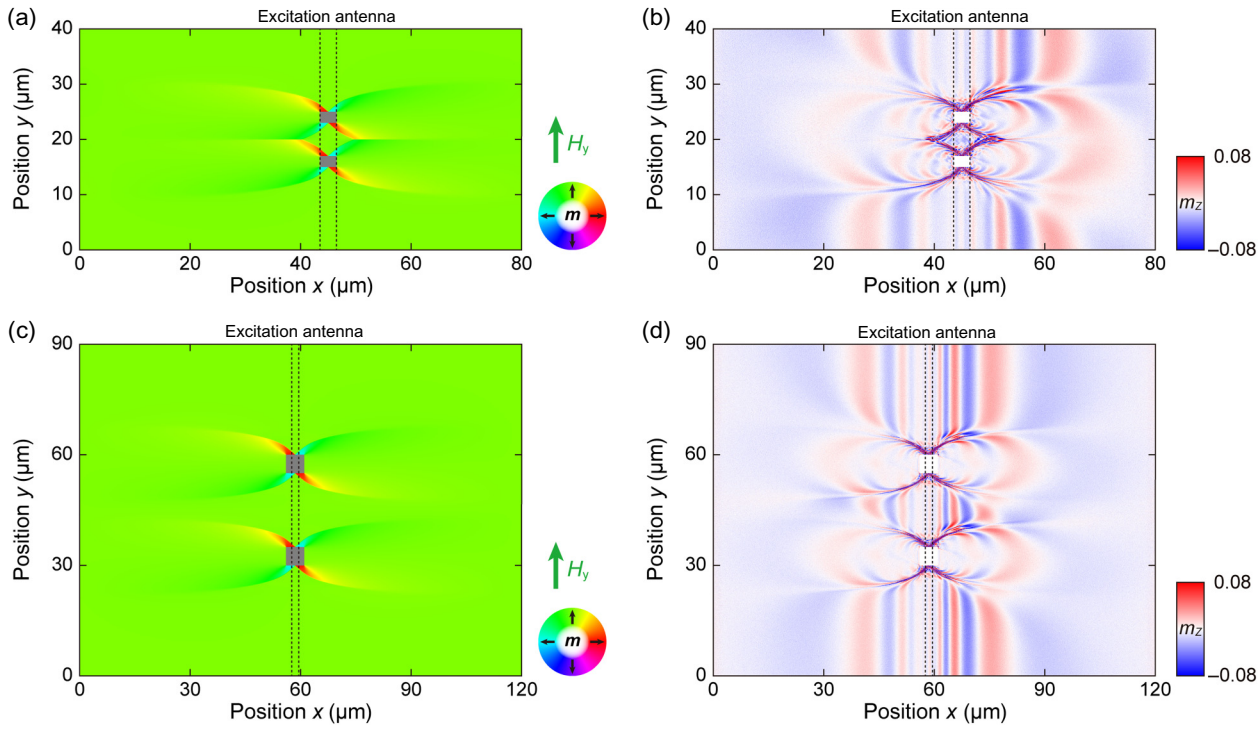

FIG. 5 Simulation of spin-wave propagation with Huygens slits. (a) Magnetization geometry of the four-port spin-wave reservoir with two Huygens slits. The dashed lines indicate the position of the excitation antenna. (b) Temporal evolution of magnetization in the Py reservoir. (c) Magnetization geometry of the eight-port spin-wave reservoir with two Huygens slits. The dashed lines indicate the position of the excitation antenna. (d) Temporal evolution of magnetization in the Py reservoir.

evaluation magnetization in the Py reservoir, as shown in Fig. 5(b). Overall, the wave fronts exhibit a spherical wave pattern. However, within the region containing the magnetic domain wall, a fine wave front pattern with distinct phases emerges. Note that the wave front of the spin wave becomes different from a simple plane wave. This observation of seemingly nonlinear behavior arises from separate measurements at multiple antenna positions. In the case of the eight-port configuration, a similar formation of a magnetic domain wall is observed, as shown in Fig. 5(c), along with the generation of distinct wave fronts within this region [Fig. 5(d)].

APPENDIX D

Micromagnetic simulations are performed by numerically solving the Landau–Lifshitz–Gilbert equation, given by $\partial \boldsymbol{m}/\partial \mathrm{t} = -\gamma_g \mu_0 \boldsymbol{m} \times \boldsymbol{H}_{\mathrm{eff}} + \alpha_G \boldsymbol{m} \times \partial \boldsymbol{m}/\partial \mathrm{t}$, where $\boldsymbol{m}$ represents the unit vector of magnetization, $\boldsymbol{H}_{\mathrm{eff}}$ denotes the effective magnetic field including exchange, magnetostatic, and external field contributions, and α_G is the Gilbert damping constant. The simulations utilize the following parameters. For the four- and eight-port spin-wave reservoirs, the dimensions are 80 μm × 40 μm × 300 nm and 120 μm × 90 μm × 300 nm, respectively. The unit cell dimensions are set at 50 nm × 50 nm × 300 nm, and the remaining parameters include the Gilbert damping constant $\alpha_G = 0.01$, the exchange stiffness constant $A_{\mathrm{exch}} = 1.6 \times 10^{-11}$ J/m, and the saturation magnetization $M_{\mathrm{s}} = 830 \times 10^3$ A/m.

[1] G. Tanaka, T. Yamane, J. B. Heroux, R. Nakane, N. Kanazawa, S. Takeda, H. Numata, D. Nakano, and A. Hirose, Recent advances in physical reservoir computing: A review, Neural Networks **115**, 100 (2019).

[2] K. Nakajima, Physical reservoir computing—an introductory perspective, Jpn. J. Appl. Phys. **59**, 060501 (2020).

[3] M. Inubushi and K. Yoshimura, Reservoir computing beyond memory-nonlinearity trade-off, Sci. Rep. **7**, 10199 (2017).

[4] H. Jaeger, The "echo state" approach to analysing and training recurrent neural networks-with an erratum note, German National Research Center for Information Technology GMD Technical Report **148**, 13 (2001).

[5] W. Maass, T. Natschilager, and H. Markram, Real-time computing without stable states: A new framework for neural computation based on perturbations, Neural Comput. **14** (11), 2531 (2002).

[6] A. F. Atiya and A. G. Parlos, New results on recurrent network training: unifying the algorithms and accelerating convergence, IEEE Trans. Neural Networks **11** (3), 697 (2000).

[7] C. Gallicchio, A. Micheli, and L. Pedrelli, Deep reservoir computing: A critical experimental analysis, Neurocomputing **268** (13), 87 (2017).

[8] Z. Li and G. Tanaka, Multi-reservoir echo state networks with sequence resampling for nonlinear time-series prediction, Neurocomputing **467** (7), 115 (2022).

[9] N. Bertschinger and T. Natschläger, Real-time computation at the edge of chaos in recurrent neural networks, Neural Comput. **16** (7), 1413 (2004).

[10] Y. Suzuki, Q. Gao, K. C. Pradel, and N. Yamamoto, Natural quantum reservoir computing for temporal information processing, Sci. Rep. **12**, 1353 (2022).

[11] R. Nakane, G. Tanaka, and A. Hirose, Reservoir computing with spin waves excited in a garnet film, IEEE Access **6**, 4462 (2018).

[12] R. Nakane, G. Tanaka, and A. Hirose, Performance enhancement of a spin-wave-based reservoir computing system utilizing different physical conditions, Phys. Rev. Appl. **19**, 034047 (2023).

[13] M. K. Lee and M. Mochizuki, Performance enhancement of a spin-wave-based reservoir computing system utilizing different physical conditions, Phys. Rev. Appl. **18**, 014074 (2022).

[14] D. Pinna, G. Bourianoff, and K. Everschor-Sitte, Reservoir computing with random skyrmion textures, Phys. Rev. Appl. **14**, 054020 (2020).

[15] K. Toprasertpong, E. Nako, Z. Wang, R. Nakane, M. Takenaka, and S. Takagi, Raw data for reservoir computing on silicon platform with a ferroelectric field-effect transistor, Commun. Eng. **1**, 21 (2022).

[16] T. Kanao, H. Suto, K. Mizushima, H. Goto, T. Tanamoto, and T. Nagasawa, Reservoir computing on spin-torque oscillator array, Phys. Rev. Appl. **12**, 024052 (2019).

[17] A. Papp, G. Csaba, and W. Porod, Characterization of nonlinear spin-wave interference by reservoir-computing metrics, Appl. Phys. Lett. **199**, 112403 (2021).

[18] D. Prychynenko, M. Sitte, K. Litzius, B. Krüger, G. Bourianoff, M. Kläui, J. Sinova, and K. Everschor-Sitte, Magnetic skyrmion as a nonlinear resistive element: a potential building block for reservoir computing, Phys. Rev. Appl. **9**, 014034 (2018).

[19] D. Markovic, N. Leroux, M. Riou, F. Abreu Araujo, J. Tor-rejon, D. Querlioz, A. Fukushima, S. Yuasa, J. Trastoy, P. Bortolotti, and J. Grollier, Reservoir computing with the frequency, phase, and amplitude of spin-torque nano-oscillators, Appl. Phys. Lett. **114**, 012409 (2019).

[20] K. Nakajima, H. Hauser, T. Li, and R. Pfeifer, Exploiting the dynamics of soft materials for machine learning, Soft Rob. **5** (3), 339 (2018).

[21] Y. K. Chembo, Machine learning based on reservoir computing with time-delayed optoelectronic and photonic systems, Chaos **30**, 013111 (2020).

[22] G. Tanaka and R. Nakane, Simulation platform for pattern recognition based on reservoir computing with memristor networks, Sci. Rep. **12**, 9868 (2022).

[23] A. G. Gurevich and G. A. Melkov, *Magnetization Oscillations and Waves* (CRC Press, London, 2020).

[24] D. D. Stancil and A. Prabhakar, *Spin Waves: Theory and Applications* (Springer, USA, 2009).

[25] A. Mahmoud, F. Ciubotaru, F. Vanderveken, A. V. Chumak, S. Hamdioui, C. Adelmann, and S. Cotofana, Introduction to spin wave computing, J. Appl. Phys. **128**, 161101 (2020).

[26] A. Papp, W. Porod, and G. Csaba, Nanoscale neural network using nonlinear spin-wave interference, Nat. Commun. **12**, 6422 (2021).

[27] S. Sunada and A. Uchida, Photonic reservoir computing based on nonlinear wave dynamics at microscale, Sci. Rep. **9**, 19078 (2019).

[28] S. Klingler, A. V. Chumak, T. Mewes, B. Khodadadi, C. Mewes, C. Dubs, O. Surzhenko, B. Hillebrands, and A. Conca, Measurements of the exchange stiffness of YIG films using broadband ferromagnetic resonance techniques, J. Phys. D: Appl. Phys. **48**, 015001 (2014).

[29] S. Miwa, M. Suzuki, M. Tsujikawa, K. Matsuda, T. Nozaki, K. Tanaka, T. Tsukahara, K. Nawaoka, M. Goto, Y. Kotani, *et al.*, Voltage controlled interfacial magnetism through platinum orbits, Nat. Commun. **8**, 15848 (2017).

[30] T. Maruyama, Y. Shiota, T. Nozaki, K. Ohta, N. Toda, M. Mizuguchi, A. A. Tulapurkar, T. Shinjo, M. Shiraishi, S. Mizukami, *et al.*, Large voltage-induced magnetic anisotropy change in a few atomic layers of iron, Nat. Nanotechnol. **4**, 158 (2009).

[31] S. Miwa, K. Matsuda, K. Tanaka, Y. Kotani, M. Goto, T. Nakamura, and Y. Suzuki, Voltage-controlled magnetic anisotropy in Fe|MgO tunnel junctions studied by x-ray absorption spectroscopy, Appl. Phys. Lett. **107**, 162402 (2015).

[32] K. Lukas, H. Christopher, H. Tobias, J. V. Kim, S. Thlang, H. Schulthelss, J. Fassbender, and K. Schultheiss, Pattern recognition in reciprocal space with a magnon-scattering reservoir, Nat. Commun. **14**, 3954 (2023).

[33] S. Nezu, T. Scheike, H. Sukegawa, and K. Sekiguchi, Propagating backward-volume spin waves in epitaxial Fe films, AIP Adv. **12**, 035320 (2022).

[34] K. Sekiguchi, S. W. Lee, H. Sukegawa, N. Sato, S. H. Oh, and R. D. McMichael, Spin-wave propagation in cubic anisotropic materials, NPG Asia Mater. **9**, e392 (2017).

[35] R. Furukawa, S. Nezu, T. Eguchi, and K. Sekiguchi, Mode-dependent magnonic noise, NPG Asia Mater. **16**, 2 (2024).

[36] R. Nakane, G. Tanaka, and A. Hirose, *Reservoir Computing High-Speed Machine Learning Theory and Hardware for Time-Series Pattern Recognition* (Morikita, Japan, 2021).

[37] T. Furuta, K. Fujii, K. Nakajima, S. Tsunegi, H. Kubota, Y. Suzuki, and S. Miwa, Macromagnetic simulation for reservoir computing utilizing spin dynamics in magnetic tunnel junctions, Phys. Rev. Appl. **10**, 034063 (2018).

[38] W. Namiki, D. Nishioka, Y. Yamaguchi, T. Tsuchiya, T. Higuchi, and K. Terabe, Experimental demonstration of high-performance physical reservoir computing with nonlinear interfered spin wave multidetection, Adv. Intell. Syst. **5**, 12 (2023).

[39] S. Watt, M. Kostylev, A. B. Ustinov, and B. A. Kalinikos, Implementing a magnonic reservoir computer model based on time-delay multiplexing, Phys. Rev. Appl. **15**, 064060 (2021).

[40] S. Watt and M. Kostylev, Reservoir computing using a spin-wave delay-line active-ring resonator based on yttrium-iron-garnet film, Phys. Rev. Appl. **13**, 034057 (2020).

[41] S. Tsunegi, T. Taniguchi, K. Nakajima, S. Miwa, K. Yakushiji, A. Fukushima, S. Yuasa, and H. Kubota, Physical reservoir computing based on spin torque oscillator with forced synchronization, Appl. Phys. Lett. **114**, 164101 (2019).

[42] A. Dejonckheere, F. Duport, A. Smerieri, L. Fang, J. Oudar, M. Haelterman, and S. Massar, All-optical reservoir computer based on saturation of absorption, Opt. Express **22** (9), 10868 (2014).

[43] P. Fan, R. Deng, J. Qiu, Z. Zhao, and S. Wu, Well logging curve reconstruction based on kernel ridge regression, Arabian J. Geosci. **14**, 1559 (2021).

[44] A. Vansteenkiste, J. Leliaert, M. Dvornik, M. Helsen, F. Garcia-Sanchez, and B. V. Waeyenberge, The design and verification of MuMax3, AIP Adv. **4**, 107133 (2014).